Growth of *c*-Axis-Oriented Superconducting KFe$_2$As$_2$ Thin Films

Hidenori Hiramatsu,*[†,‡] Shogo Matsuda,[†] Hikaru Sato,[†] Toshio Kamiya,[†,‡] and Hideo Hosono[†,‡,§]

[†]Materials and Structures Laboratory, Tokyo Institute of Technology, Mailbox R3-1, 4259 Nagatsuta-cho, Midori-ku, Yokohama 226-8503, Japan

[‡]Materials Research Center for Element Strategy, Tokyo Institute of Technology, Mailbox S2-16, 4259 Nagatsuta-cho, Midori-ku, Yokohama 226-8503, Japan

[§]Frontier Research Center, Tokyo Institute of Technology, Mailbox S2-13, 4259 Nagatsuta-cho, Midori-ku, Yokohama 226-8503, Japan

Ⓢ *Supporting Information*

ABSTRACT: KFe$_2$As$_2$, an iron-based superconductor, is expected to exhibit large spin Hall conductivity, and fabrication of high-quality thin films is requisite for evaluation of this effect and application to spintronics devices. Thin-film growth of KFe$_2$As$_2$ is difficult because of two intrinsic properties; its extremely hygroscopic nature and the high vapor pressure of potassium. We solved these issues by combining room-temperature pulsed laser deposition using K-rich KFe$_2$As$_2$ targets with thermal crystallization in KFe$_2$As$_2$ powder after encapsulation in an evacuated silica-glass tube with all of the processes conducted in a vacuum chamber and a dry Ar atmosphere in a glovebox. The optimized KFe$_2$As$_2$ films on (La,Sr)(Al,Ta)O$_3$ single-crystal substrates were obtained by crystallization at 700 °C, and they were strongly *c*-axis oriented. The electrical measurements were performed with thin films protected by grease passivation to block reaction with the atmosphere. The KFe$_2$As$_2$ films exhibited a superconductivity transition at 3.7 K.

KEYWORDS: iron-based superconductors, air-sensitive materials, potassium, thin films, pulsed laser deposition, thermal annealing
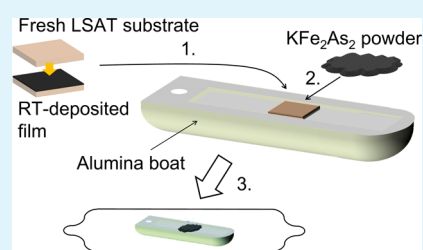
1. INTRODUCTION

The reports on superconductivity of the 1111-type layered iron-pnictides, LaFePO[1] and LaFeAsO,[2] immediately invoked discovery of superconductivity in other iron-based compounds such as 122-type BaFe$_2$As$_2$,[3] 111-type LiFeAs,[4] and 11-type FeSe.[5] The maximum critical temperature (T_c) reaches 55 K for F-[6] or H-doped[7] SmFeAsO. Because of the attractive superconducting properties, such as high upper critical fields (H_{c2}) well above 50 T,[8,9] small anisotropy factors ($\gamma = H_{c2}^{//ab}/H_{c2}^{//c} = 1-2$ for the 122-type compounds[9]), and an advantageous grain-boundary nature,[10] as well as the high T_c, thin-film growth techniques have made great progress[11–13] since the report of the heteroepitaxial growth of LaFeAsO films.[14] At present, self-field critical current densities exceed 1 MA/cm^2 for films on metal-tape flexible substrates.[15,16]

A novel attractive property has recently been theoretically predicted for KFe$_2$As$_2$. Pandey et al.[17] reported that KFe$_2$As$_2$, which is the end member of 122-type (Ba$_{1-x}$K$_x$)Fe$_2$As$_2$ (i.e., $x = 1$) with $T_c \approx 3$ K,[18,19] may exhibit a large spin Hall conductivity (SHC) comparable to that of Pt.[20] That is, 10^4 times larger SHC (2×10^4 $(\Omega m)^{-1}$) than that of a semiconductor (0.5 $(\Omega m)^{-1}$).[21] Such a high SHC originates from strong spin–orbit coupling of the Fe 3d states with Dirac cones below the Fermi level of heavily hole-doped KFe$_2$As$_2$. Indeed, high-resolution angle-resolved photoemission spectroscopy experiments showed that the electron pocket at the M point of (Ba$_{1-x}$K$_x$)Fe$_2$As$_2$ completely disappeared for KFe$_2$As$_2$ because of its heavily self-hole-doped nature (Ba^{2+} ↔ K$^+$ + hole).[22]

For semiconductors with weak spin–orbit coupling,[23,24] optical detection techniques are commonly used to measure the spin Hall effect because their spin diffusion lengths are much larger than the spot size of the laser light ($\sim$1 μm). However, optical techniques are difficult to apply to systems with nanometer-scale spin diffusion lengths because of strong spin–orbit interactions. Therefore, detection of the SHC in KFe$_2$As$_2$ is not possible with bulk single crystals and requires high-quality nanometer-scale thin films. Additionally, the SHC should be investigated with nanometer-scale devices smaller than the diffusion length to observe the SHC signal similar to the case of Pt, where the spin diffusion length is extremely short at $\sim$10 nm.[25]

Because KFe$_2$As$_2$ contains the alkali metal K as a main constituent, it is very air sensitive. Therefore, growth, electrical measurements, and device patterning of KFe$_2$As$_2$ thin films are all challenging issues, although there are reports of the synthesis of polycrystalline and single-crystal bulk samples.[18,19,26–31] Mainly owing to their air sensitivity, there is only one report of the growth of a KFe$_2$As$_2$ film, which used molecular beam epitaxy.[32] A very weak *c*-axis orientation of the film was reported, but its chemical composition was unclear and no superconductivity was confirmed.

In this study, we investigated several methods to grow 122-type KFe_2As_2 films using pulsed laser deposition (PLD) and postdeposition thermal annealing. We used the following approaches: Method (I): room temperature (RT) direct deposition using stoichiometric KFe_2As_2 targets to examine the effects of re-evaporation of constituent elements without additional K supply. Method (II): high-temperature direct deposition using K-rich KFe_2As_2 targets. Method (III): K supply from a Knudsen cell (K-cell) was added to Method (II). Method (IV): thermal annealing of films deposited at RT using K-rich targets. Three thermal annealing processes were investigated for Method (IV): (IVa) crystallization with additional K supplied from KFe_2As_2 powder, (IVb) greater K supply than (IVa) by thermal chemical transfer using K lump, and (IVc) solid-phase crystallization of thin films covered with a single-crystal substrate and buried in KFe_2As_2 powder. Best KFe_2As_2 films were obtained by Method (IVc) and of strong c-axis orientation with weak epitaxial relation in the a−b plane, exhibiting a superconductivity transition at 3.7 K.

2. EXPERIMENTAL SECTION

2.1. Synthesis of Precursors and Polycrystalline KFe_2As_2 Disks. The precursor compounds (KAs, K_3As, and Fe_2As) used to make the stoichiometric KFe_2As_2 and K-rich KFe_2As_2 disks for PLD targets were synthesized by solid-state reactions. To synthesize the KAs and K_3As precursors, a K metal block kept in an oil (purity: 99.5%, size: $40 \times 30 \times 20$ mm^3, Sigma-Aldrich) was rinsed with dehydrated-heptane in air and then rapidly moved into a glovebox with a dry and inert Ar atmosphere (dew point <−90 °C, oxygen concentration <1 ppm). The thin oxidized layer on the top surface of the K block was carefully removed and then the block was cut into small blocks with sizes of approximately $5 \times 5 \times 5$ mm^3. The cut K and As (grains, purity: 99.9999%, Kojundo Chemical Laboratory) were mixed to molar ratios of K/As = 1:1 for KAs and 3:1 for K_3As. The mixture was then sealed in a stainless tube, which was dried in advance in the glovebox for at least 1 day under the inert atmosphere. Temperature of the sealed stainless tube was elevated at 400 °C for 20 h and then maintained at 400 °C for 20 h to complete the chemical reaction between K and As. For the Fe_2As precursor, a stoichiometric mixture of Fe powder (purity: 99.9% up, Kojundo Chemical Laboratory) and As grains was sealed in an evacuated silica-glass ampule followed by heating at 750 °C for 16 h.

The KFe_2As_2 and K-rich KFe_2As_2 PLD target disks (size: ~8 mm in diameter and ~5 mm thick, density: ~80%) were synthesized by solid-state reactions. For the KFe_2As_2 disks, the precursors KAs and Fe_2As were mixed with the stoichiometric composition (KAs + Fe_2As → KFe_2As_2). For the K-rich KFe_2As_2 disks, the precursors K_3As and Fe_2As were mixed with a well-dried silica-glass mortar at a molar ratio of K_3As/Fe_2As = 1:1. The mixture was then sealed in a stainless tube and heated at 700 °C for 16 h to complete the chemical reaction of the precursors. The resulting powders were ground and uniaxially pressed into disks, which were sealed in stainless tubes and then heated at 500 °C for 10 h to prevent loss of K during this final sintering process.

All of the above fabrication processes, except for the sealing process of the stoichiometric mixtures for the Fe_2As precursor in the silica-glass ampules and the heating process of the stainless tubes and silica-glass ampules in the furnaces, were performed in the dry and inert atmosphere glovebox.

2.2. Thin-Film Growth. *2.2.1. PLD as a Common Process (Methods (I)−(IV)).* Thin films with 100−200 nm thickness were grown on (001)-oriented mixed-perovskite type $(La,Sr)(Al,Ta)O_3$ single-crystal substrates (LSAT, area: 10×10 mm^2, thickness: 0.5 mm) by PLD in vacuum using a KrF excimer laser (COMPex*Pro* 110, Coherent Inc., wavelength: 248 nm, repetition rate: 10 Hz). LSAT was chosen because the in-plane lattice mismatch between KFe_2As_2 (the a-axis lattice parameter $a = 0.384$ nm) and LSAT (a/2 = 0.387 nm) is small (+0.8%). The LSAT substrates were annealed at 1000 °C for 30 min in an ambient atmosphere to remove contaminants and improve

the surface morphology prior to the film deposition. The laser fluence and substrate temperature (T_s) were varied between 1.7 and 4.3 J/cm^2 and RT and 560 °C, respectively. The base pressures of the PLD growth chamber and the preparation/load lock chamber connected to the glovebox were $\sim 1 \times 10^{-7}$ and $\sim 1 \times 10^{-5}$ Pa, respectively. Hereafter, RT and high-T_s in situ direct deposition are categorized as Methods (I) and (II), respectively.

2.2.2. Method (III): Additional K Supplied by K-Cell. For Method (III), we used a K-cell to supply additional K flux during the PLD growth at high T_s, where In_8K_5 alloy grains[33] synthesized by solid-state reaction of a stoichiometric mixture of In and K at 490 °C for 12 h were filled in a BN crucible, and then heated at $T_{K\text{-cell}}$ = 200 and 350 °C. The corresponding K fluxes, which were monitored in advance with a beam flux monitor at the deposition position, were $\sim 1 \times 10^{-3}$ and $\sim 5 \times 10^{-2}$ Pa for $T_{K\text{-cell}}$ = 200 and 350 °C, respectively. In_8K_5 was used to obtain pure K flux because In_8K_5 is much more chemically stable in air than K, which allows it to be treated in air for a short time when we put it into the BN crucible of the K-cell. In addition, the vapor pressure of K ($\sim 7 \times 10^2$ Pa at 650 K) is much higher than that of In ($\sim 10^{-9}$ Pa at 650 K),[34] and more pure K flux than the K metal source case can be easily obtained.

2.2.3. Method (IV): Solid-phase Crystallization. We also investigated three postdeposition thermal annealing processes to crystallize films deposited at T_s = RT using K-rich PLD targets. All of the as-deposited films were transferred from the preparation chamber of the PLD to the glovebox in Ar atmosphere, in which all the preparation procedures for the following thermal annealing processes were conducted.

Methods (IVa)−(IVc) used an additional K supply from KFe_2As_2 powder or K lump, because the addition of an excess of a high vapor pressure element, such as alkali metals, is effective to compensate for the vaporization loss during thermal annealing.[35−37] The annealing temperature (T_a) was varied from 350 to 800 °C. The experimental setups used for Methods (IVa)−(IVc) are shown schematically in Figure 1(a)−(c), respectively.

2.2.3.1. Method (IVa): Crystallization with Additional K Supply from KFe_2As_2 Powder. Method (IVa) is similar to the method for obtaining polycrystalline films of layered chalcogenides such as LaCuO(S,Se) and BaCuFS.[38−40] The as-deposited films at RT were sealed in evacuated silica-glass ampules with large amounts of KFe_2As_2 powder, and then the ampules were thermally annealed (see Figure 1(a)).

2.2.3.2. Method (IVb): Crystallization with Additional K Supply from K Lump. Method (IVb) used a greater K supply from a K lump and higher temperatures (T_K) than Method (IVa). The film temperature (T_{film}) and T_K were independently controlled (See Figure 1(b)).

2.2.3.3. Method (IVc): Crystallization with the Thin Film Covered with a Single-Crystal Substrate and Buried in KFe_2As_2 Powder. For Method (IVc), the surface of the as-deposited film was covered with a fresh LSAT plate to prevent evaporation during annealing,[36,37,41−44] and the covered sample was buried in a large amount of KFe_2As_2 powder in an alumina boat. The alumina boat was sealed in an evacuated silica-glass ampule, and then thermally annealed (see Figure 1(c)).

2.3. Characterization. The crystalline phases of the films were determined by conventional X-ray diffraction (XRD, source: Cu Kα radiated from a rotational anode, θ−2θ synchronous scan with Bragg−Brentano geometry), which is appropriate for detecting a small amount of impurity and nonoriented crystallites because of the stronger diffraction intensity and higher sensitivity than high-resolution XRD. The fluctuations of the crystallite orientations were characterized using the rocking curves of out-of-plane (2θ-fixed ω scans) diffractions with a high-resolution XRD apparatus (source: Cu Kα_1 monochromated by Ge(220)). The in-plane orientation of the films was investigated using a pole figure geometry. All of the XRD measurements were performed using an O-ring sealed sample-holder filled with dry Ar gas to prevent degradation of the samples during the measurements.
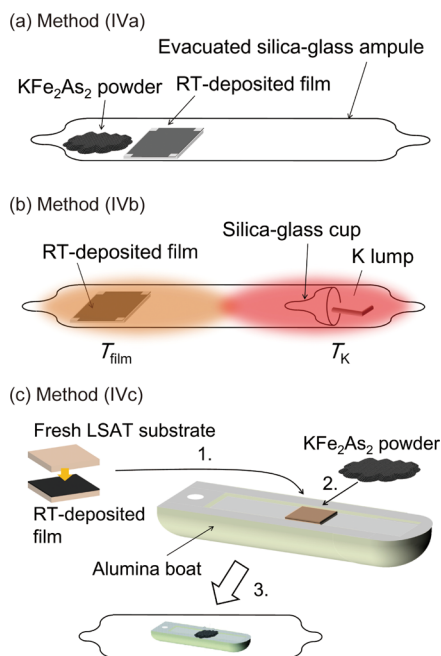
Figure 1. Schematic illustration of the experimental setup for the postdeposition thermal annealing processes of Method (IV) for RT-deposited films in evacuated silica-glass ampules. (a) Method (IVa): thermal annealing with KFe_2As_2 powder. (b) Method (IVb): thermal annealing with K lump. The annealing temperatures at the film position (T_{film}) and K lump (T_K) were controlled independently. (c) Method (IVc): the surface of the as-deposited film was covered with another fresh LSAT substrate, and then it was transferred to an alumina boat. Large amounts of KFe_2As_2 powder were then placed on the fresh LSAT substrate.

The chemical compositions of the films were determined with an energy dispersive X-ray spectroscopy (EDX) apparatus equipped with a field-emission scanning electron microscope (FE-SEM), and an electron probe microanalyzer (EPMA) using wavelength dispersive spectroscopy mode. The quantitative analyses were conducted using the atomic number, absorption, fluorescence (ZAF) correction method with the standard references of $KTiPO_5$ for K, LaAs for As, and Fe for Fe. The sample surface was covered with a thin Au film deposited in situ in the PLD chamber before transferring from the glovebox to the analysis apparatuses.

The microstructure of the obtained KFe_2As_2 films, whose surface was protected with thin Au films, was observed by transmission electron microscopy (TEM) and high-angle annular dark field scanning TEM (HAADF-STEM). The distribution of the chemical composition in the films was investigated by an EDX apparatus equipped with a STEM. We confirmed that the results obtained by the EPMA quantitative analyses using the ZAF correction method agreed well with those obtained by semiquantitative analysis of FE-SEM/STEM EDX. To prepare the TEM/STEM samples, we used an atmosphere-blocking attachment for a focused ion beam apparatus (FIB) in the glovebox. Using this attachment, we transferred the samples from the glovebox to the FIB, and then to the TEM/STEM load lock chambers under inert atmosphere without exposure to air.

The temperature (T) dependences of the in-plane electrical resistivity (ρ) were measured by the four-probe method using an alternating dc current applied parallel to the film plane (i.e., perpendicular to the c-axis of the KFe_2As_2 films) in the T range 2–300 K with a physical property measurement system (PPMS, Quantum Design). External magnetic fields (H) were applied normal to the substrate (i.e., parallel to the c-axis of the c-axis-oriented films). After in situ deposition of the Au electrodes by PLD at RT with a shadow mask and wiring of the electrodes in the glovebox, the surface of the sample was completely covered with grease (Apiezon N, M&I

Materials Ltd.) to protect it from the atmosphere, and then it was immediately transferred from the glovebox to the PPMS measurement chamber under ambient air.

3. RESULTS AND DISCUSSION

3.1. Chemical Composition of Films Deposited by PLD at RT (Method (I)). To evaluate the transferability of the chemical composition from the PLD target to a film via the laser ablation process, we measured the chemical composition of films deposited at RT from the stoichiometric KFe_2As_2 target by EPMA (see Supporting Information (SI) Figure S1 for XRD pattern of the stoichiometric KFe_2As_2 target). In general, it is believed that the chemical composition of the PLD target will be the same as the film if re-evaporation from the film is negligible, e.g., at low temperatures such as RT. Figure 2(a)
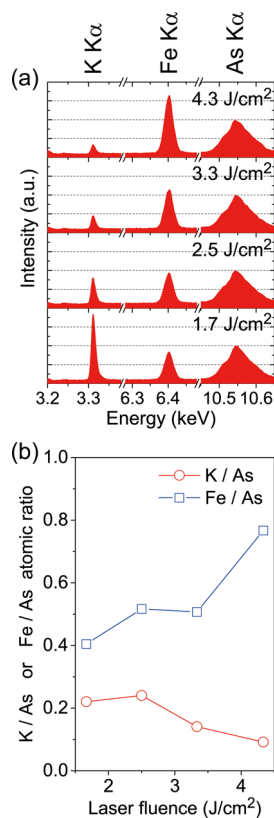

Figure 2. Laser fluence dependence of the chemical compositions of films deposited by PLD at T_s = RT using the stoichiometric KFe_2As_2 PLD target (Method (I)). (a) EPMA spectra of constituent elements for films deposited at 1.7–4.3 J/cm^2. (b) K/As and Fe/As atomic ratios obtained from (a) as a function of laser fluence.

shows the EMPA spectra of the constituent elements of the films deposited at laser fluences of 1.7–4.3 J/cm^2, and Figure 2(b) summarizes the atomic composition ratios of K/As and Fe/As. The As concentration is almost the same in each film. However, the K and Fe concentrations vary with the fluence despite RT deposition: all the K/As ratios are much lower than the stoichiometric value (0.5) and decreased with increasing fluence. This result indicates that all the films are K-poor and exact chemical transfer of K from the PLD target is difficult even if deposited at RT. In contrast, the Fe/As ratio increased with increasing fluence, but still showed Fe-poor compositions (i.e., Fe/As < 1.0) in the whole examined fluence region. That is, higher fluence is better to obtain Fe/As ratios closer to the

ideal value (1.0) but worse for the K composition. We chose the fluence $\sim$3 J/cm^2 from the viewpoint of the best available balance, although the K and Fe concentrations in the films were as low as $\sim$50% of the stoichiometric compositions. This indicates that we have to compensate their losses by supplying additional K and Fe during postdeposition crystallization to produce the KFe_2As_2 phase when a stoichiometric KFe_2As_2 PLD target is used. Because of this reason, we used K-rich KFe_2As_2 (i.e., $K_3As/Fe_2As = 1:1$) disks as the PLD targets in Methods (II)−(IV).

3.2. Film Growth by PLD at High T_s (Methods (II) and (III)). Figure 3 shows XRD patterns of the films deposited at T_s
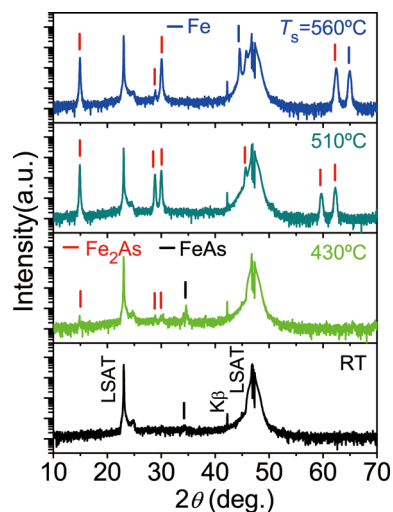
Figure 3. XRD patterns of films deposited by PLD using K-rich KFe_2As_2 targets at T_s = RT − 560 °C (Method (II)).

= RT−560 °C using K-rich KFe_2As_2 PLD targets without K supply from the K-cell (Methods (II)). When deposited at T_s = RT, the obtained films were almost amorphous, as judged from a weak halo around 2θ = 20−30° (the weak diffraction peak comes from the impurity FeAs phase). When deposited at T_s = 430 °C, Fe_2As and FeAs phases were observed. With further increase in T_s, single-phase Fe_2As films were obtained at T_s = 510 °C, and then Fe began to appear at T_s = 560 °C. This result indicates that the KFe_2As_2 crystalline phase is not formed for T_s ≥ 430 °C because of the complete loss of K, which is confirmed by EDX (the bottom pattern in Figure 4(b)). This result indicates that K in the film re-evaporates from the growing surface during PLD deposition at high T_s, and the impurity phases of FeAs, Fe_2As, and Fe are segregated in this order as T_s increased owing to their thermal stabilities.

Next, we used a K-cell with the In_8K_5 alloy as an additional K source during the PLD growth (Method (III)). Figure 4(a) shows the XRD patterns of the films at different T_{K-cell} and T_s. At T_{K-cell} = 200 °C and T_s = 300 °C (the bottom pattern in Figure 4(a)), a diffraction peak from the FeAs phase was observed. With further increase in T_{K-cell} and T_s to 350 and 340 °C (the upper pattern in Figure 4(a)), the diffraction peak from FeAs became sharper, while the KFe_2As_2 phase was not formed, even though the K flux at T_{K-cell} = 340 °C is 50 times greater than that at T_{K-cell} = 200 °C. To verify the incorporation of K in the films, Figure 4(b) compares the EDX spectra of three types of film deposited at T_s = 430 °C (bottom panel), T_{K-cell} = 350 °C and T_s = 340 °C (middle panel), and T_s = RT (top panel). In the case of the film deposited at T_s = 430 °C, no signal of K
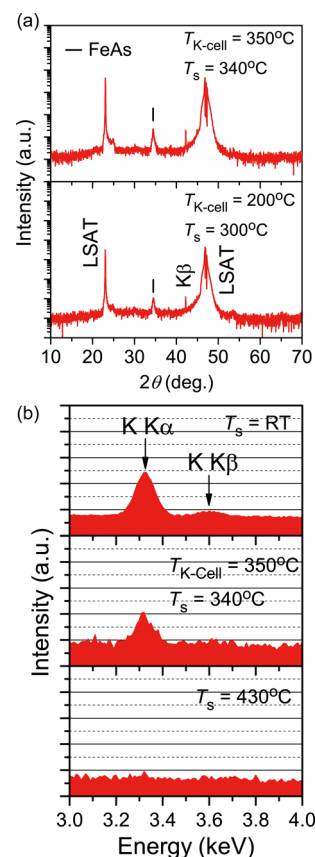
Figure 4. (a) XRD patterns of the films deposited by PLD using K-rich KFe_2As_2 targets at different T_{K-cell} and T_s (Method (III)). (b) EDX spectra of the three types of films deposited at different T_s and/or T_{K-Cell} in the region of the K $K\alpha$ and $K\beta$ lines (3−4 keV).

was observed, which is consistent with the result obtained by the XRD measurements in Figure 3 (the films were a mixture of Fe_2As and FeAs phases). The crystalline phase of the films using the K-cell during PLD growth was the FeAs phase, although a K $K\alpha$ signal was observed in the EDX spectrum (middle panel of Figure 4(b)). This result indicates that the K-cell was effective in supplying additional K flux during PLD growth but an even higher T_s is required to crystallize the films in the KFe_2As_2 phase. However, the K concentration was still lower than that deposited at T_s = RT (the top panel of Figure 4(b)) and the stoichiometric value. Therefore, we conclude that it is difficult to grow crystalline KFe_2As_2 thin films by a simple in situ PLD process even with a K-cell.

3.3. Thermal Annealing of Films Deposited by PLD at RT (Method (IV)). According to the above results, the maximum K concentration is obtained by RT deposition for the simple PLD process. Therefore, we performed postdeposition thermal annealing by Methods (IVa)−(IVc) for the as-deposited films at RT using the K-rich KFe_2As_2 PLD targets (See Figure 1).

3.3.1. Method (IVa): Crystallization with KFe_2As_2 Powder. Figure 5 shows the XRD patterns of the films annealed by Method (IVa) (see Figure 1(a)). The approach of Method (IVa) is effective to grow layered chalcogenides such as LaCuOS and BaCuSF, which have layered crystal structures similar to KFe_2As_2 and are similar in terms of chemical stability where off-stoichiometry of Cu and S easily occurs during thermal annealing.[38−40] When annealed at T_a = 500 °C
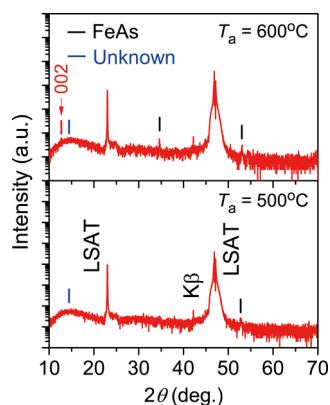
Figure 5. XRD patterns of the films annealed by Method (IVa) at T_a = 500 °C (lower panel) and 600 °C (upper panel).

(bottom panel in Figure 5), we observed a broad diffraction peak at around $2\theta = 14°$ along with diffraction peaks from the FeAs impurity phase and the LSAT substrate. The broad peak at ~14° has a 2θ value higher than that of the KFe$_2$As$_2$ 002 diffraction peak, which should appear at $2\theta = 12.76°$. At T_a = 600 °C (upper panel in Figure 5), the FeAs diffraction peak became sharper than at 500 °C, while a very weak diffraction peak was observed at $2\theta \approx 12.8°$, which can be assigned to KFe$_2$As$_2$ 002 diffraction. However, with increasing T_a from 500 to 600 °C, the unknown phase at about $2\theta = 14°$ remained, and the FeAs phase became dominant.

3.3.2. Method (IVb): Crystallization with K Lump by Independent Control of T_{film} and T_K. Next, we investigated Method (IVb) (see Figure 1(b)). Figure 6(a) summarizes the crystalline phases of the films annealed at different T_{film} and T_K. In the low T_{film} region (region (i) in Figure 6(a)), the obtained films were amorphous (the bottom pattern in Figure 6(b)) because only a weak halo around $2\theta = 20-30°$ was observed apart from the diffraction peaks from the LSAT substrate. In the higher T_{film} region (region (ii) in Figure 6(a)), a broad diffraction peak was observed at about $2\theta = 12.7°$, which can be assigned to KFe$_2$As$_2$ 002 diffraction (see the middle pattern in Figure 6(b)). We attempted to measure the full width at half-maximum (fwhm) of the out-of-plane rocking curve of the diffraction peak, but the measured width (>6°) exceeded the measurement limit of the ω axis in this 2θ region. This weak c-axis orientation is comparable to a film grown by molecular beam epitaxy reported in ref 32, where a higher 00l diffraction series, such as l = 4, 6, and 8, was not observed. Because no diffraction peaks other than those from LSAT were observed, we performed a pole figure measurement for the 103 diffraction of KFe$_2$As$_2$ to further confirm the KFe$_2$As$_2$ phase and in-plane orientation (see SI Figure S2). At this geometry, we observed a ring ϕ-pattern centered at about $\psi = 50°$, indicating that the obtained film was weakly c-axis-oriented KFe$_2$As$_2$ with random in-plane orientation. Additionally, the EDX semiquantitative analysis (K/Fe/As = 19:41:40, approximately 1:2:2) further supports that this sample is the KFe$_2$As$_2$ phase. With further increase in T_{film} (region (iii) in Figure 6(a)), the 002 diffraction peak completely disappeared and diffractions of Fe$_2$As and FeAs were observed despite the high T_K = 700 °C, as shown in the top pattern in Figure 6(b). We independently changed T_{film} and T_K to separate the crystallization region and K evaporation region, but found that the crystallization region only depended on T_{film} (Figure 6(a)). That is, independent control of T_K was not effective to control the K concentration in the films, which
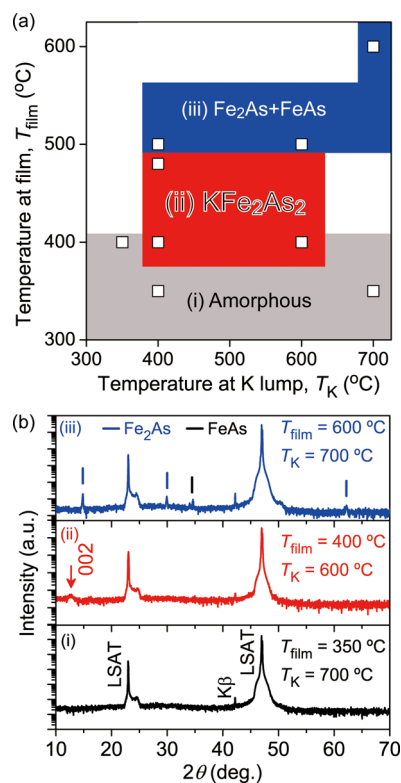

Figure 6. Variation in the precipitated crystalline phases prepared by Method (IVb). (a) Crystalline phase map of the films annealed at different T_{film} and T_K. The investigated conditions are shown by open squares. (b) Representative XRD patterns of regions (i)–(iii) in (a).

indicates that the K concentration in the film is limited by the thermal evaporation rate determined by T_{film}. Additionally, the obtained films did not show superconductivity even at the lowest measured T of 2 K (see SI Figure S3), which is similar to a polycrystalline KFe$_2$As$_2$ bulk.[19]

3.3.3. Method (IVc): Annealing of Films Buried in KFe$_2$As$_2$ Powder. On the basis of the results obtained by Methods (IVa) and (IVb), we considered that high T_a was necessary to obtain high-crystallinity KFe$_2$As$_2$ films. Thus, we used Method (IVc) (see Figure 1(c)) to supply K to the films during the high T_a annealing. Figure 7(a) shows the XRD patterns of the films annealed at T_a = 500−800 °C by Method (IVc). At T_a = 500 °C, we observed 002 and 103 (main peak) diffractions of KFe$_2$As$_2$ along with those of the LSAT substrate. At T_a = 600 °C, the c-axis orientation became stronger than at 500 °C. It is noteworthy that all the 00l series diffractions (l = 2, 4, 6, 8, and 10) were clearly observed on the films annealed at T_a = 700 °C, although a weak 103 diffraction was also detected at $2\theta = 30.2°$. This result indicates that the films are strongly c-axis oriented for the out-of-plane diffraction. The fwhm of the out-of-plane 002 diffraction was 0.4° (Figure 7(b)). The c-axis lattice parameter (1.382 nm) is consistent with the reported values.[18,19,26,29] At T_a = 800 °C, crystalline KFe$_2$As$_2$ remained as a minor phase, and diffractions from Fe$_2$As, FeAs, and Fe became dominant, indicating evaporation of K dominated at 800 °C despite the KFe$_2$As$_2$ powder completely covering the sample.

From the above results, we conclude that the optimum method among Methods (IVa)−(IVc) is Method (IVc) at T_a = 700 °C. However, the 103 pole figure (Figure 7(c)) of the KFe$_2$As$_2$ film annealed at T_a = 700 °C by Method (IVc) shows
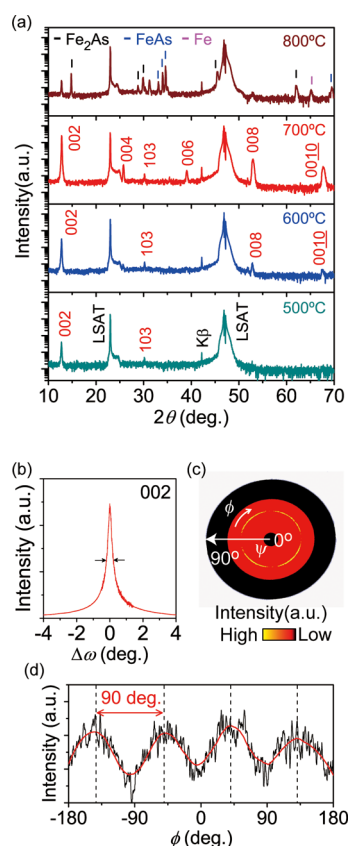
Figure 7. (a) XRD patterns of the films annealed at T_a = 500−800 °C buried in KFe_2As_2 powder (Method (IVc)). (b) Out-of-plane rocking curve of 002 diffraction of the KFe_2As_2 film annealed at T_a = 700 °C. (c) Pole figure of 103 diffraction of the KFe_2As_2 film annealed at T_a = 700 °C. (d) Cross-section of (c) at the ψ scan peak ∼50°. The red line is smoothed from the raw data.

a similar ring pattern at about ψ = 50° as that obtained by Method (IVb) (see SI Figure S2). However, as shown in Figure 7(d), broad periodic diffraction was observed every 90°, indicating that the films were also weakly oriented in-plane and grew semiepitaxially.

3.4. Microstructure and Chemical Composition of the KFe_2As_2 Films.

We investigated the microstructure and composition distribution of the KFe_2As_2 films obtained by

Method (IVc) at T_a = 700 °C. Figure 8(a) shows a cross-sectional HAADF-STEM image. The surface has a roughness of several tens of nanometers. In the bulk region of the film, there is not a clear contrast except domain/grain boundary regions, suggesting that the composition is uniform. The composition ratios of K/As and Fe/As in the films annealed by Method (IVc) became of almost stoichiometric ones although K-poor and Fe-rich films were obtained for the deposited films at high T_s (Methods (II) − (III), Figures 3−5). However, as shown in Figure 8(b) (see SI Figure S4 for the EDX spectra for each position in (a)), the surface regions 2 and 6 in Figure 8(a) have a Fe-poor composition, while the K concentration is uniform and almost at the stoichiometric value of K/As = 0.5. As shown in SI Figure S4(b), the intensity of the O $K\alpha$ peak at 0.525 eV is extremely weak. This result confirms that the sample was successfully transferred from the glovebox to the FIB/TEM/STEM without exposure to air. Additionally, we observed a different contrast at the KFe_2As_2 film−LSAT substrate interface, as shown in the magnified image in Figure 8(c). Figure 8(c),(d) shows the HAADF-STEM image and compositions at the interface, respectively (see SI Figure S5 for the EDX spectra corresponding to the positions in (c)). Compared with position 7 in Figure 8(c) (the bulk region in the film), the interface has a K-rich and Fe-poor composition. To examine the atomic structure at the interface, we used high-resolution TEM (Figure 8(e)). We observed a layered structure in the film region, and its interlayer distance was equal to that of the (002) plane (i.e., half of the c-axis) of KFe_2As_2. Note that an amorphous-like interfacial layer ∼10 nm thick was formed. Similar interface reaction layers are also formed in thin films of the iron-based superconductor $Ba(Fe,Co)_2As_2$.[45−48] The origin of these reaction layers is still unclear, but it would be an important factor to improve these iron pnictide superconductor films. This result also suggests that LSAT substrate is not the best one for epitaxial growth of high-quality films, and we may choose other single-crystal substrates with larger lattice mismatches.

3.5. Superconductivity.

Figure 9(a) shows the $\rho-T$ curve of the KFe_2As_2 films grown by Method (IVc) at T_a = 700 °C. The normal state resistivity at 300 K was 1.5×10^{-2} Ω cm, which is 2 orders of magnitude higher than that of single crystal (3.0×10^{-4} Ω cm).[29] This is presumably because of the domain/grain boundaries observed in Figure 8(a). Accordingly, the residual resistivity ratio (RRR, $\rho(300$ K$)/\rho(5$ K$)$) was ∼20,
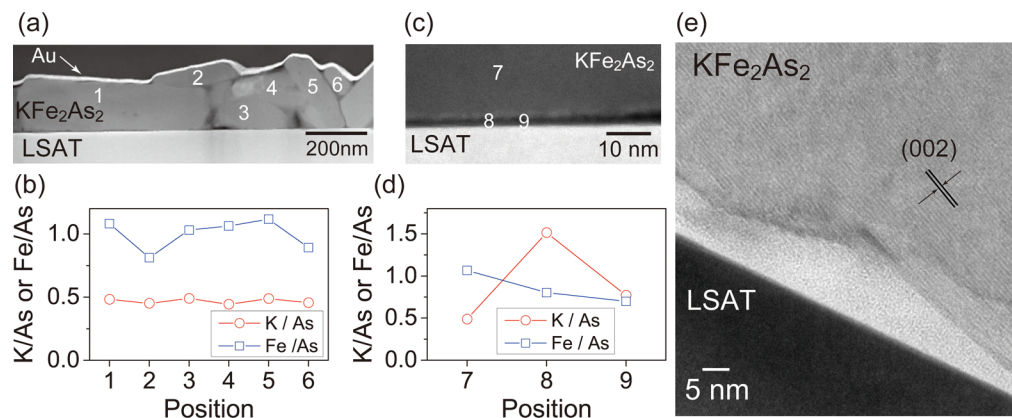

Figure 8. Cross-sectional microstructure and chemical composition of KFe_2As_2 films grown by Method (IVc) at T_a = 700 °C. (a) HAADF-STEM image. (b) Chemical compositions at the positions numbered in (a). (c) HAADF-STEM image at the interface between the KFe_2As_2 film and LSAT substrate. (d) Chemical compositions at the positions numbered in (c). (e) High-resolution TEM image at the interface.
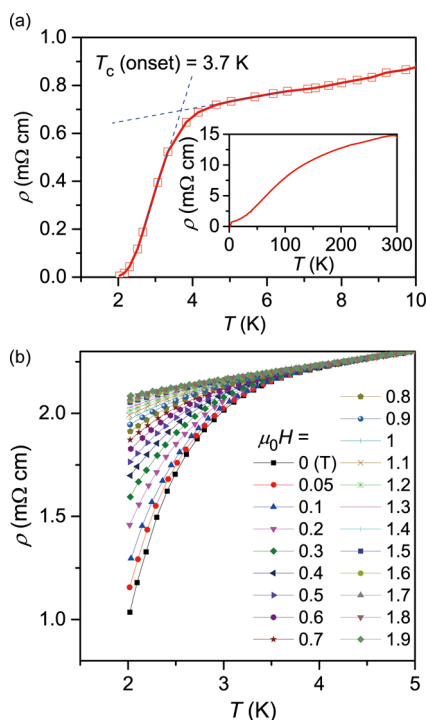
Figure 9. (a) $\rho-T$ curves of KFe$_2$As$_2$ films grown by Method (IVc) at $T_a = 700$ °C. The inset shows that the wider T range of 2−300 K. (b) External magnetic field (H) dependence of the $\rho-T$ curves for $\mu_0 H = 0$−1.9 T.

which is much smaller than that of single crystals (RRR = 87,[27] 86,[28] 458,[29] and 3000[30]). We observed the onset T_c at 3.7 K, which is similar to that of a single crystal,[29] and a clear zero resistivity was observed at 2 K.

To confirm the superconductivity, we applied H parallel to the c-axis (Figure 9(b)). Here, the absolute value of ρ was slightly higher than the above $\rho-T$ measurement (Figure 9(a)). This observation indicates that the film surface region was slightly degraded even though the sample surface was covered by grease (Apiezon N) and rapidly transferred to PPMS from the glovebox. We also investigated other protection layers, including pure polystyrene in solvents (Q-Dope, GC Electronics), which has been found to be effective for (Ba$_{1-x}$K$_x$)Fe$_2$As$_2$ ($x < 1$),[32] and an epoxy adhesive (Nitofix SK-229; Nitto Shinko Co.), and found that Apiezon N grease provided the best protection. Despite the slight degradation, we observed a clear T_c shift to lower temperatures with increasing H. Additionally, a clear suppression of the superconductivity was observed at $\mu_0 H = 1.9$ T. The Werthamer−Helfand−Hohenberg formula[49] gives $H_{c2}^{//c} \approx 3$ T. This is slightly higher than that of single crystals (~1 T), and may be due to the weak in-plane orientation because $H_{c2}^{//ab}$ (4−5 T) is higher than $H_{c2}^{//c}$.[27,30,31]

4. CONCLUSIONS

We investigated the growth of KFe$_2$As$_2$ films as a first step to investigate the large SHC that has been recently theoretically predicted for KFe$_2$As$_2$. Although K-rich PLD targets and a K-cell as an additional K source were used, in situ PLD growth at high T_s was unsuccessful mainly because of K re-evaporation during growth. Therefore, we investigated three types of postdeposition thermal annealing processes for as-deposited films at T_s = RT. Annealing with KFe$_2$As$_2$ powder in the

evacuated silica-glass ampules was insufficient to obtain single-phase KFe$_2$As$_2$ films, but using K lump to efficiently supply K in the ampules resulted in the growth of weakly c-axis-oriented KFe$_2$As$_2$ films at the optimum T_{film}. Covering the films with KFe$_2$As$_2$ powder during annealing was the most effective method to prevent re-evaporation of K among all the methods considered in this study, leading to strongly c-axis-oriented KFe$_2$As$_2$ films being obtained. Consequently, despite its air sensitivity, a clear superconducting transition at $T_c = 3.7$ K was observed in the resulting strongly c-axis-oriented films.

■ ASSOCIATED CONTENT

S **Supporting Information**

XRD pattern of the stoichiometric KFe$_2$As$_2$ disk, pole figure, and temperature dependence of the resistance for the KFe$_2$As$_2$ film grown at $T_{film} = 400$ °C and $T_K = 600$ °C, EDX spectra of the KFe$_2$As$_2$ film grown by Method (IVc) at $T_a = 700$ °C. This material is available free of charge via the Internet at http://pubs.acs.org.

■ AUTHOR INFORMATION

Corresponding Author
*E-mail: h-hirama@lucid.msl.titech.ac.jp.

Notes
The authors declare no competing financial interest.

■ ACKNOWLEDGMENTS

■ REFERENCES

(1) Kamihara, Y.; Hiramatsu, H.; Hirano, M.; Kawamura, R.; Yanagi, H.; Kamiya, T.; Hosono, H. Iron-Based Layered Superconductor: LaOFeP. *J. Am. Chem. Soc.* **2006**, *128*, 10012−10013.

(2) Kamihara, Y.; Watanabe, T.; Hirano, M.; Hosono, H. Iron-Based Layered Superconductor La[O$_{1-x}$F$_x$]FeAs ($x = 0.05$−0.12) with $T_c = 26$ K. *J. Am. Chem. Soc.* **2008**, *130*, 3296−3297.

(3) Rotter, M.; Tegel, M.; Johrendt, D. Superconductivity at 38 K in the Iron Arsenide (Ba$_{1-x}$K$_x$)Fe$_2$As$_2$. *Phys. Rev. Lett.* **2008**, *101*, 107006.

(4) Wang, X. C.; Liu, Q. Q.; Lv, Y. X.; Gao, W. B.; Yang, L. X.; Yu, R. C.; Li, F. Y.; Jin, C. Q. The Superconductivity at 18 K in LiFeAs System. *Solid State Commun.* **2008**, *148*, 538−540.

(5) Hsu, F.-C.; Luo, J.-Y.; Yeh, K.-W.; Chen, T.-K.; Huang, T.-W.; Wu, P. M.; Lee, Y.-C.; Huang, Y.-L.; Chu, Y.-Y.; Yan, D.-C.; Wu, M.-K. Superconductivity in the PbO-Type Structure α-FeSe. *Proc. Natl. Acad. Sci. U.S.A.* **2008**, *105*, 14262−14264.

(6) Ren, Z.-A.; Lu, W.; Yang, J.; Yi, W.; Shen, X.-L.; Li, Z.-C.; Che, G.-C.; Dong, X.-L.; Sun, L.-L.; Zhou, F.; Zhao, Z.-X. Superconductivity at 55K in Iron-Based F-Doped Layered Quaternary Compound Sm[O$_{1-x}$F$_x$]FeAs. *Chin. Phys. Lett.* **2008**, *25*, 2215−2216.

(7) Hanna, T.; Muraba, Y.; Matsuishi, S.; Igawa, N.; Kodama, K.; Shamoto, S.-i.; Hosono, H. Hydrogen in Layered Iron Arsenides: Indirect Electron Doping to Induce Superconductivity. *Phys. Rev. B* **2011**, *84*, 024521.

(8) Hunte, F.; Jaroszynski, J.; Gurevich, A.; Larbalestier, D. C.; Jin, R.; Sefat, A. S.; McGuire, M. A.; Sales, B. C.; Christen, D. K.; Mandrus, D. Two-Band Superconductivity in LaFeAsO$_{0.89}$F$_{0.11}$ at Very High Magnetic Fields. *Nature* **2008**, *453*, 903−905.

(9) Yamamoto, A.; Jaroszynski, J.; Tarantini, C.; Balicas, L.; Jiang, J.; Gurevich, A.; Larbalestier, D. C.; Jin, R.; Sefat, A. S.; McGuire, M. A.; Sales, B. C.; Christen, D. K.; Mandrus, D. Small Anisotropy, Weak Thermal Fluctuations, and High Field Superconductivity in Co-Doped Iron Pnictide Ba(Fe$_{1−x}$Co$_x$)$_2$As$_2$. *Appl. Phys. Lett.* **2009**, *94*, 062511.

(10) Katase, T.; Ishimaru, Y.; Tsukamoto, A.; Hiramatsu, H.; Kamiya, T.; Tanabe, K.; Hosono, H. Advantageous Grain Boundaries in Iron Pnictide Superconductors. *Nat. Commun.* **2011**, *2*, 409.

(11) For a review Li, Q.; Si, W.; Dimitrov, I. K. Films of Iron Chalcogenide Superconductors. *Rep. Prog. Phys.* **2011**, *74*, 124510.

(12) For a review Hiramatsu, H.; Katase, T.; Kamiya, T.; Hosono, H. Thin Film Growth and Device Fabrication of Iron-Based Superconductors. *J. Phys. Soc. Jpn.* **2012**, *81*, 011011.

(13) For a review Haindl, S.; Kidszun, M.; Oswald, S.; Hess, C.; Büchner, B.; Kölling, S.; Wilde, L.; Thersleff, T.; Yurchenko, V. V.; Jourdan, M.; Hiramatsu, H.; Hosono, H. Thin Film Growth of Fe-Based Superconductors: From Fundamental Properties to Functional Devices. A Comparative Review. *Rep. Prog. Phys.* **2014**, *77*, 046502.

(14) Hiramatsu, H.; Katase, T.; Kamiya, T.; Hirano, M.; Hosono, H. Heteroepitaxial Growth and Optoelectronic Properties of Layered Iron Oxyarsenide, LaFeAsO. *Appl. Phys. Lett.* **2008**, *93*, 162504.

(15) Katase, T.; Hiramatsu, H.; Matias, V.; Sheehan, C.; Ishimaru, Y.; Kamiya, T.; Tanabe, K.; Hosono, H. Biaxially Textured Cobalt-Doped BaFe$_2$As$_2$ Films with High Critical Current Density over 1 MA/cm^2 on MgO-Buffered Metal-Tape Flexible Substrates. *Appl. Phys. Lett.* **2011**, *98*, 242510.

(16) Si, W.; Han, S. J.; Shi, X.; Ehrlich, S. N.; Jaroszynski, J.; Goyal, A.; Li, Q. High Current Superconductivity in FeSe$_{0.5}$Te$_{0.5}$-Coated Conductors at 30 T. *Nat. Commun.* **2013**, *4*, 1347.

(17) Pandey, S.; Kontani, H.; Hirashima, D. S.; Arita, R.; Aoki, H. Spin Hall Effect in Iron-Based Superconductors: A Dirac-Point Effect. *Phys. Rev. B* **2012**, *86*, 060507.

(18) Sasmal, K.; Lv, B.; Lorenz, B.; Guloy, A. M.; Chen, F.; Xue, Y.-Y.; Chu, C.-W. Superconducting Fe-Based Compounds (A$_{1−x}$Sr$_x$)-Fe$_2$As$_2$ with A = K and Cs with Transition Temperatures up to 37 K. *Phys. Rev. Lett.* **2008**, *101*, 107007.

(19) Rotter, M.; Pangerl, M.; Tegel, M.; Johrendt, D. Superconductivity and Crystal Structures of (Ba$_{1−x}$K$_x$)Fe$_2$As$_2$ (x = 0−1). *Angew. Chem., Int. Ed.* **2008**, *47*, 7949−7952.

(20) Kimura, T.; Otani, Y.; Sato, T.; Takahashi, S.; Maekawa, S. Room-Temperature Reversible Spin Hall Effect. *Phys. Rev. Lett.* **2007**, *98*, 156601.

(21) Stern, N. P.; Ghosh, S.; Xiang, G.; Zhu, M.; Samarth, N.; Awschalom, D. D. Current-Induced Polarization and the Spin Hall Effect at Room Temperature. *Phys. Rev. Lett.* **2006**, *97*, 126603.

(22) Sato, T.; Nakayama, K.; Sekiba, Y.; Richard, P.; Xu, Y.-M.; Souma, S.; Takahashi, T.; Chen, G. F.; Luo, J. L.; Wang, N. L.; Ding, H. Band Structure and Fermi Surface of an Extremely Overdoped Iron-Based Superconductor KFe$_2$As$_2$. *Phys. Rev. Lett.* **2009**, *103*, 047002.

(23) Kato, Y. K.; Myers, R. S.; Gossard, A. C.; Awschalom, D. D. Observation of the Spin Hall Effect in Semiconductors. *Science* **2004**, *306*, 1910−1913.

(24) Wunderlich, J.; Kaestner, B.; Sinova, J.; Jungwirth, T. Experimental Observation of the Spin-Hall Effect in a Two-Dimensional Spin-Orbit Coupled Semiconductor System. *Phys. Rev. Lett.* **2005**, *94*, 047204.

(25) Kurt, H.; Loloee, R.; Eid, K.; Pratt, W. P., Jr.; Bass, J. Spin-Memory Loss at 4.2 K in Sputtered Pd and Pt and at Pd/Cu and Pt/Cu Interfaces. *Appl. Phys. Lett.* **2002**, *81*, 4787−4789.

(26) Chen, H.; Ren, Y.; Qiu, Y.; Bao, W.; Liu, R. H.; Wu, G.; Wu, T.; Xie, Y. L.; Wang, X. F.; Huang, Q.; Chen, X. H. Coexistence of the Spin-Density Wave and Superconductivity Ba$_{1−x}$K$_x$Fe$_2$As$_2$. *EPL* **2009**, *85*, 17006.

(27) Terashima, T.; Kimata, M.; Satsukawa, H.; Harada, A.; Hazama, K.; Uji, S.; Harima, H.; Chen, G.-F.; Luo, J.-L.; Wang, N.-L. Resistivity and Upper Critical Field in KFe$_2$As$_2$ Single Crystals. *J. Phys. Soc. Jpn.* **2009**, *78*, 063702.

(28) Dong, J. K.; Zhou, S. Y.; Guan, T. Y.; Zhang, H.; Dai, Y. F.; Qiu, X.; Wang, X. F.; He, Y.; Chen, X. H.; Li, S. Y. Quantum Criticality and Nodal Superconductivity in the FeAs-Based Superconductor KFe$_2$As$_2$. *Phys. Rev. Lett.* **2010**, *104*, 087005.

(29) Kihou, K.; Saito, T.; Ishida, S.; Nakajima, M.; Tomioka, Y.; Fukazawa, H.; Kohori, Y.; Ito, T.; Uchida, S.; Iyo, A.; Lee, C.-H.; Eisaki, H. Single Crystal Growth and Characterization of the Iron-Based Superconductor KFe$_2$As$_2$ Synthesized by KAs Flux Method. *J. Phys. Soc. Jpn.* **2010**, *79*, 124713.

(30) Liu, Y.; Tanatar, M. A.; Kogan, V. G.; Kim, H.; Lograsso, T. A.; Prozorov, R. Upper Critical Field of High-Quality Single Crystals of KFe$_2$As$_2$. *Phys. Rev. B* **2013**, *87*, 134513.

(31) Abdel-Hafiez, M.; Aswartham, S.; Wurmehl, S.; Grinenko, V.; Hess, C.; Drechsler, S.-L.; Johnston, S.; B. Wolter, A. U.; Büchner, B.; Rosner, H.; Boeri, L. Specific Heat and Upper Critical Fields in KFe$_2$As$_2$ Single Crystals. *Phys. Rev. B* **2012**, *85*, 134533.

(32) Yamagishi, T.; Ueda, S.; Takeda, S.; Takano, S.; Mitsuda, A.; Naito, M. A Study of the Doping Dependence of T_c in Ba$_{1−x}$K$_x$Fe$_2$As$_2$ and Sr$_{1−x}$K$_x$Fe$_2$As$_2$ Films Grown by Molecular Beam Epitaxy. *Phys. C (Amsterdam, Neth.)* **2011**, *471*, 1177−1180.

(33) Takeda, S.; Ueda, S.; Yamagishi, T.; Agatsuma, S.; Takano, S.; Mitsuda, A.; Naito, M. Molecular Beam Epitaxy Growth of Superconducting Sr$_{1−x}$K$_x$Fe$_2$As$_2$ and Ba$_{1−x}$K$_x$Fe$_2$As$_2$. *Appl. Phys. Express* **2010**, *3*, 093101.

(34) *CRC Handbook of Chemistry and Physics*, 82nd ed.; CRC Press: Boca Raton, FL, 2001, Section 4, p 134.

(35) Watari, K.; Hwang, H. J.; Toriyama, M.; Kanzaki, S. Effective Sintering Aids for Low-Temperature Sintering of AlN Ceramics. *J. Mater. Res.* **1999**, *14*, 1409−1417.

(36) Kamiya, T.; Ohta, H.; Kamiya, M.; Nomura, K.; Ueda, K.; Hirano, M.; Hosono, H. Li-Doped NiO Epitaxial Thin Film with Atomically Flat Surface. *J. Mater. Res.* **2004**, *19*, 913−920.

(37) Ohta, H.; Kim, S.-W.; Ohta, S.; Koumoto, K.; Hirano, M.; Hosono, H. Reactive Solid-Phase Epitaxial Growth of Na$_x$CoO$_2$ (x ≈ 0.83) via Lateral Diffusion of Na into a Cobalt Oxide Epitaxial Layer. *Cryst. Growth Des.* **2005**, *5*, 25−28.

(38) Ueda, K.; Inoue, S.; Hirose, S.; Kawazoe, H.; Hosono, H. Transparent p-Type Semiconductor: LaCuOS Layered Oxysulfide. *Appl. Phys. Lett.* **2000**, *77*, 2701−2703.

(39) Hiramatsu, H.; Orita, M.; Hirano, M.; Ueda, K.; Hosono, H. Electrical Conductivity Control in Transparent p-Type (LaO)CuS Thin Films Prepared by RF Sputtering. *J. Appl. Phys.* **2002**, *91*, 9177−9181.

(40) Park, C.-H.; Keszler, D. A.; Yanagi, H.; Tate, J. Gap Modulation in MCu[Q$_{1−x}$Q′$_x$]F (M = Ba, Sr; Q, Q′ = S, Se, Te) and Related Materials. *Thin Solid Films* **2003**, *445*, 288−293.

(41) Hiramatsu, H.; Ueda, K.; Ohta, H.; Orita, M.; Hirano, M.; Hosono, H. Heteroepitaxial Growth of a Wide-Gap p-Type Semiconductor, LaCuOS. *Appl. Phys. Lett.* **2002**, *81*, 598−600.

(42) Ohta, H.; Nomura, K.; Orita, M.; Hirano, M.; Ueda, K.; Suzuki, T.; Ikuhara, Y.; Hosono, H. Single-Crystalline Films of the Homologous Series InGaO$_3$(ZnO)$_m$ Grown by Reactive Solid-Phase Epitaxy. *Adv. Funct. Mater.* **2003**, *13*, 139−144.

(43) Hiramatsu, H.; Ohta, H.; Suzuki, T.; Honjo, C.; Ikuhara, Y.; Ueda, K.; Kamiya, T.; Hirano, M.; Hosono, H. Mechanism for Heteroepitaxial Growth of Transparent p-Type Semiconductor: LaCuOS by Reactive Solid-Phase Epitaxy. *Cryst. Growth Des.* **2004**, *4*, 301−307.

(44) Hiramatsu, H.; Ueda, K.; Takafuji, K.; Ohta, H.; Hirano, M.; Kamiya, T.; Hosono, H. Fabrication of Heteroepitaxial Thin Films of Layered Oxychalcogenides LnCuOCh (Ln = La−Nd; Ch = S−Te) by Reactive Solid-Phase Epitaxy. *J. Mater. Res.* **2004**, *19*, 2137−2143.

(45) Iida, K.; Hänisch, J.; Thersleff, T.; Kurth, F.; Kidszun, M.; Haindl, S.; Hühne, R.; Schultz, L.; Holzapfel, B. Scaling Behavior of

the Critical Current in Clean Epitaxial $Ba(Fe_{1-x}Co_x)_2As_2$ Thin Films. *Phys. Rev. B* **2010**, *81*, 100507.

(46) Rall, D.; Il'in, K.; Iida, K.; Haindl, S.; Kurth, F.; Thersleff, T.; Schultz, L.; Holzapfel, B.; Siegel, M. Critical Current Densities in Ultrathin $Ba(Fe,Co)_2As_2$ Microbridges. *Phys. Rev. B* **2011**, *83*, 134514.

(47) Ichinose, A.; Tsukada, I.; Nabeshima, F.; Imai, Y.; Maeda, A.; Kurth, F.; Holzapfel, B.; Iida, K.; Ueda, S.; Naito, M. Induced Lattice Strain in Epitaxial Fe-Based Superconducting Films on CaF_2 Substrates: A Comparative Study of the Microstructures of SmFeAs-(O,F), $Ba(Fe,Co)_2As_2$, and $FeTe_{0.5}Se_{0.5}$. *Appl. Phys. Lett.* **2014**, *104*, 122603.

(48) Hiramatsu, H.; Sato, H.; Katase, T.; Kamiya, T.; Hosono, H. Critical Factor for Epitaxial Growth of Cobalt-Doped $BaFe_2As_2$ Films by Pulsed Laser Deposition. *Appl. Phys. Lett.* **2014**, *104*, 172602.

(49) Werthamer, N. R.; Helfand, E.; Hohenberg, P. C. Temperature and Purity Dependence of the Superconducting Critical Field, H_{c2}. III. Electron Spin and Spin-Orbit Effects. *Phys. Rev.* **1966**, *147*, 295−302.